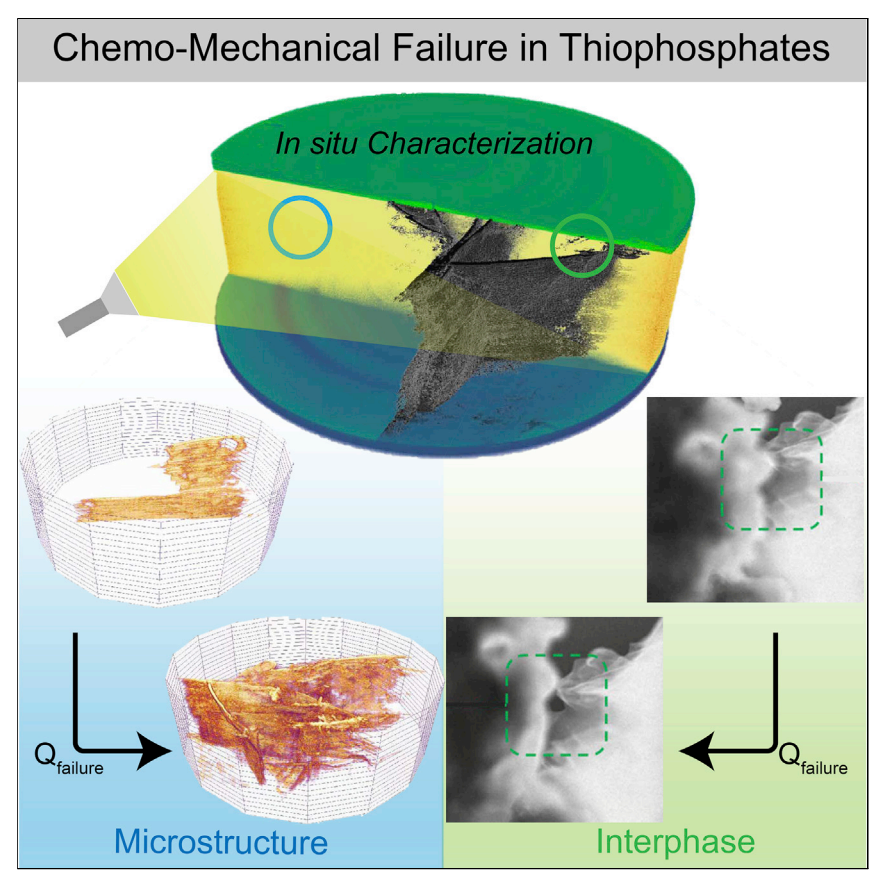
Matter



Article

In Situ Investigation of Chemomechanical Effects in Thiophosphate Solid Electrolytes



Solid electrolytes can realize high-energy-density batteries by use of a lithium metal anode. However, filament growth and electrolyte fracture limit the solid-state battery performance. In this work, we investigate the impact of interphase chemistry and microstructure on chemomechanical degradation of thiophosphate solid electrolytes. Achieving metastable interphases and dense solid electrolytes are key to high-energy-density solid-state batteries.

Marm B. Dixit, Nikhilendra Singh, James P. Horwath, ..., Eric A. Stach, Timothy S. Arthur, Kelsey B. Hatzell

tim.arthur@toyota.com (T.S.A.) kelsey.b.hatzell@vanderbilt.edu (K.B.H.)

HIGHLIGHTS

Chemomechanical effects in thiophosphate solid electrolytes investigated

Halide addition leads to metastable interphase by I⁻ diffusion to anode interface

Electrochemistry-driven interfacial chipping phenomenon identified as crack onset

Microstructural anisotropy dictates failure propagation through solid electrolyte

Matter



Article

In Situ Investigation of Chemomechanical Effects in Thiophosphate Solid Electrolytes

Marm B. Dixit,^{1,8} Nikhilendra Singh,^{2,8} James P. Horwath,³ Pavel D. Shevchenko,⁴ Michael Jones,² Eric A. Stach,^{3,5} Timothy S. Arthur,^{2,*} and Kelsey B. Hatzell^{1,6,7,9,*}

SUMMARY

Solid-state batteries can suffer from catastrophic failure at high current densities due to solid electrolyte fracture, interface decomposition, or lithium filament growth. Failure is linked to chemomechanical material transformations that can manifest during electrochemical cycling. We systematically investigate how solid electrolyte microstructure and interfacial decomposition (e.g., interphase) affect failure mechanisms in lithium thiophosphates (Li₃PS₄, LPS) electrolytes. Kinetically metastable interphases are engineered with iodine doping, and microstructural control is achieved using milling and annealing processing techniques. In situ transmission electron microscopy reveals iodine diffusion to the interphase, and upon electrochemical cycling, pores are formed in the interphase region. In situ synchrotron tomography reveals that interphase pore formation drives edge fracture events, which are the origin of through-plane fracture failure. Fractures in thiophosphate electrolytes actively grow toward regions of higher porosity and are affected by heterogeneity in microstructure (e.g., porosity factor). This work provides fundamental design guidelines for high-performance solid-state batteries.

INTRODUCTION

All-solid-state batteries can enable energy-dense anodes for next-generation energy-storage systems.^{1,2} Solid electrolytes, such as thio-LISICONs, lithium-phosphorus-sulfur (LPS) glasses, and argyrodites (Li_6PS_5X , X = Cl, Br, I), with high ionic conductivity (>10⁻³ S cm⁻¹) and low electronic conductivity ($\sigma_e \approx nS cm^{-1}$)^{3,4} are especially promising for lithium (Li) metal solid-state batteries. However, despite excellent transport properties, the electrode|solid electrolyte chemomechanical stability remains a significant challenge. ^{2,5} Most inorganic solid electrolytes are reactive with Li metal and form an interfacial decomposition product or interphase region. There are three prominent types of Li|SE interphases: (1) thermodynamically or kinetically stable (non-reactive), (2) unstable (reactive), ^{6,7} and (3) kinetically metastable (Figure 1A).^{8,9} Few solid electrolytes are non-reactive with Li metal, with Garnettype LLZO ($\text{Li}_7\text{La}_3\text{Zr}_2\text{O}_{12}$) being a possible exception. ^{10,11} NASICON-type solid electrolytes (e.g., LAGP, LATGP) are examples of reactive electrolytes that form a mixed (ionic/electronic) conductivity interphase. ⁶ Finally, several types of solid electrolytes are metastable and form an interphase that is electronically insulating and ionically conducting. Li₃PS₄, for example, is kinetically metastable, as the interphase is primarily composed of electrically insulating lithium sulfide (Li₂S) and lithium phosphide (Li₃P).^{7,8,12} While interphase structure, composition, and properties are not well understood, interphase growth leads to greater cell polarization. 13,14 The

Progress and Potential

Li filament growth and solid electrolyte fracture are key technical challenges limiting the commercial application of solidstate batteries. Electrical shorting, irreversible Li cycling, and the formation of dead Li at high current density limits the Coulombic efficiency and rate capability of solid electrolytes. A fundamental understanding regarding fracture mechanisms will inform materials design and system operating strategies for next-generation solid-state batteries. This work leverages advanced characterization techniques to investigate material transformation pathways in sulfide-containing solid electrolytes. We highlight the importance of microstructural heterogeneity in dictating degradation in solid electrolytes and offer insight into fracture onset and growth mechanisms. These results offer vital information required to rationally engineer solid-state battery systems that can mitigate Li filament growth and enable high energy density and high rate capability.





microstructure and transport properties of the interphase can lead to non-uniform current densities, low power density, and local stress generation at buried electrode|electrolyte interfaces. ^{15,16,17} The latter can result in catastrophic failure via Li filament formation, electrical shorting, and fracture. ¹⁸

Active or passive approaches during electrolyte synthesis and processing are commonly utilized to control interphase properties. Active approaches include the use of an interlayer barrier film. 19-22 Prior studies have investigated atomic layer deposition of interlayer materials (Al₂O₃, Si, Li_xAl_(2-x/3)O, LiXO₃ [X = Ta, Nb]) to improve the surface wetting capability of metallic Li and lower interfacial resistances. 11,23,24 Passive approaches such as halide doping or substitution have been reported to increase the stability of sulfide-containing electrolytes with Li metal through the formation of a nanometer-thin passivating interphase.^{25,26} Halide doping has also been reported to improve the ionic conductivity, wettability with the Li metal, and the electrochemical stability window. 4,19,27-32 Theoretical and experimental studies ascribe this increase in performance to the formation of an ionically conducting interphase with Li₂S, Li₃P, and Lil. ¹⁹ While transport in the interphase undoubtedly plays a role in performance, it is less clear how the chemomechanics of the interphase governs performance. Stress within individual battery components and/or at interfaces can occur because of physical volume change, ^{5,33} the formation of gas, 34,35 and/or mass (ion) transport. 36-38 While concentration gradients do not exist in a single ion-conducting electrolyte, there is the potential for stress-assisted diffusion at solid|solid interfaces.³⁸ Irregular interphase growth or Li⁰ electrodeposition can lead to stress gradients in a solid electrolyte, and alter the local energy level of the cation and contribute to directed ionic transport. 36,39 Mechanical stresses can also affect the dissolution and deposition kinetics governed by molar volume mismatch between solid electrolyte and Li metal electrode.³⁶ These chemomechanical effects can lead to non-uniform ionic flux at electrode|solid electrolyte interface and be a driver for mechanical degradation. Several competing hypotheses are proposed for chemomechanical degradation and failure of solid electrolytes. 40,41 Unstable interphase formation due to reactivity between solid electrolyte and Li metal can cause mechanical stresses at the interface and cause fracture. 13 Trace electrical conduction in the solid electrolyte can cause isolated Li deposition, which can subsequently grow through a connected pore network causing failure. 42,43 Interfacial compatibility and irreversible electrode volume change can also cause chemomechanical degradation of solid electrolytes.⁴¹ Preferential filling of local flaws and subsequent filament growth through the flaws can lead to fracture within the solid electrolyte. 15 Modeling studies have highlighted that chemical and geometric defects at a Li|SE interface can cause decohesion of Li and/or fracture of SE. 44,45 Pressure buildup at dendrite tips are shown by coupled transport, and plastic and elastic deformation models to exceed hundreds of MPa, which can potentially cause fracture. 46-48 In situ characterization of morphological changes in SE are required to assess the failure mechanisms.

The interdependent relationship between local ion transport, electrode|electrolyte contact, and solid electrolyte mechanical properties and cycle life is important for resilient solid-state batteries. Thiophosphate solid electrolytes with halide substitution and/or doping have lower Young's modulus that can enable stress-accommodating interfaces, better contact with metallic Li, and longer cycle lifetime. ⁴⁹ In the absence of excess Li, the anode undergoes a 100% change in thickness. While exact estimation of the associated strain on the electrolyte corresponding to this variation is difficult, a qualitative comparison of mechanical response for solid electrolytes with low and high Young's modulus can be made. Compliant interfaces, i.e.,

https://doi.org/10.1016/j.matt.2020.09.018

¹Department of Mechanical Engineering, Vanderbilt University, Nashville, TN 37235, USA

²Toyota Research Institute of North America, Ann Arbor, MI 48105, USA

³Department of Material Science and Engineering, University of Pennsylvania, Philadelphia, PA 19104, USA

⁴X-Ray Science Division, Argonne National Laboratory, Lemont, IL 60439, USA

⁵Laboratory for Research on the Structure of Matter, University of Pennsylvania, Philadelphia, PA 19104, USA

⁶Interdisciplinary Department of Material Science, Vanderbilt University, Nashville, TN 37235 1154

⁷Department of Chemical and Biomolecular Engineering, Vanderbilt University, Nashville, TN 37235, USA

⁸These authors contributed equally

⁹Lead Contact

^{*}Correspondence: tim.arthur@toyota.com (T.S.A.), kelsey.b.hatzell@vanderbilt.edu (K.B.H.)





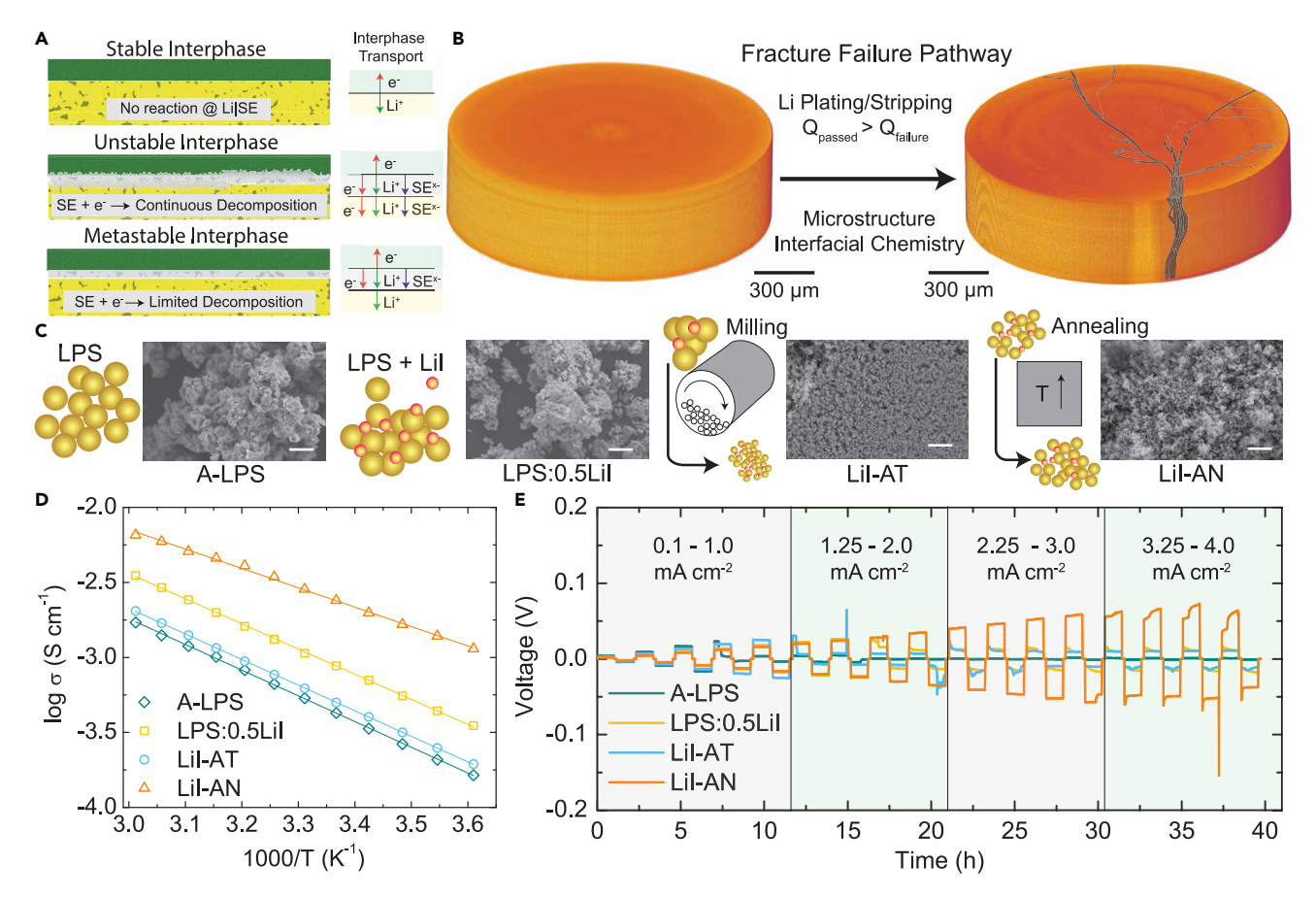


Figure 1. Electrochemical Characterization and Materials Transformations Pathways Observed in Thiophosphate Solid Electrolytes

(A) Schematic diagram depicting Li metal and solid electrolyte interphase types. Stable interphase has no chemical decomposition of SE; unstable interphase shows continuous SE decomposition while kinetically metastable interphase shows controlled SE decomposition. Corresponding ionic and electronic conduction behavior is also indicated.

(B) 3D tomography reconstruction of pristine and failed LPS electrolyte pellet. Effect of interfacial chemistry and microstructure on mechanical failure in LPS materials is investigated.

(C) SEM images of powder materials in the study along with schematic diagrams highlighting processing used to synthesize the material. The scale bar on all images represents 10 μ m. A-LPS is amorphous sulfide material. LPS:0.5Lil is a mixture of amorphous LPS and Lil salt. Lil-AT material is obtained by mechanical milling of the LPS:0.5Lil material. Lil-AN is obtained by annealing the Lil-AT material.

(D and E) (D) Ionic conductivity and (E) critical current density measurement for the solid electrolytes. See Figures S1–S4.

interfaces that maintain contact when subject to electrochemical stresses during cycling, require dissipation of the stresses within the material. In solid electrolytes with low Young's modulus (18 GPa 50), the stresses generated by Li metal electrode-position/electrodissolution can be accommodated by the solid electrolyte by deformation. This potentially can enable conformal deposition/stripping of Li metal at the interface. In contrast, with a high-modulus material, the non-compliant nature of the solid electrolyte (low deformation to electrodeposition/electrodissolution stress) can lead to non-planar morphologies in the anode, leading to instabilities. However, thiophosphate solid electrolytes have low fracture toughness (\approx 0.2 MPa m $^{1/2}$) and are prone to fracture. 50,51 It should be noted that mechanical response of the Li electrode is generally in the flow/creep regime 52 and, additionally, molar volume mismatch of Li $^{+}$ and Li metal 5,36 can impart electrochemical stresses at the interface. Prior work on the NASICON family of solid electrolytes has suggested that interphase instability can lead to non-uniform stress distribution, which initiates





fracture-induced failure.⁵³ Other works suggest that operating conditions^{54–56} or the bulk solid electrolyte^{15,42,43,57–59} may be origins of fracture. Volume changes arising from electrodeposition and electrodissolution of Li metal can lead to stress generation at the interphase. Additionally, mechanical stresses can arise from volume changes derived from chemical decomposition of the solid electrolyte, as well as molar volume mismatch between Li⁺ and Li metal. All of these factors can also contribute to mechanical failure of the solid electrolytes.

The influence of electrolyte microstructure heterogeneity on stress distribution and fracture mechanics is not well known. This lack in understanding is primarily because there are limited experimental techniques capable of probing these dynamics at buried interfaces. One technique capable of in situ characterization of solid-state batteries is synchrotron X-ray computed tomography (XCT), which offers resolutions of \sim 1 μm . This resolution range is ideal for the detection of mesoscale material transformations in solid-state batteries.⁶⁰ Recently, ex situ studies revealed that pore connectivity in garnet-type oxides was correlated with obtainable critical current densities. 43,61 Furthermore, XCT has revealed that mechanical deformation and irregular contact at electrode|electrolyte interfaces may drive filament propagation in Na⁺ β-alumina and LPS electrolytes, respectively. 62,63 Failure mechanisms transcend several length scales, from nanoscale interfacial reactions to mesoscale crack and fracture propagation. Furthermore, these occur at disparate time scales, thus complicating experimental assessment.⁶⁴ Combining electrochemical measurements with (non-destructive) characterization techniques is crucial for deconvoluting the nature of chemomechanics in solid-state battery systems.⁶⁵

Here, we systematically study material transformation pathways that affect fracture in a series of thiophosphate solid electrolytes in order to understand the nature of interphase chemistry and microstructural heterogeneity on fracture. Thiophosphate solid electrolytes are systematically altered for interfacial chemistry (via halogen doping) and microstructural heterogeneity (milling and annealing). A multimodal approach is employed to elucidate the role of solid electrolyte microstructure and interphase in affecting fracture events. In situ transmission electron microscopy (TEM) provides evidence for interphase formation mechanisms and provides nanoscale insight into pore formation in the interphase, which drives edge fracture degradation modes at solid electrolyte|lithium interfaces. In situ synchrotron XCT experiments resolve fracture growth mechanisms. Fracture pathways in solid electrolyte are correlated with microstructure heterogeneities. The results demonstrate that the temporal onset of fracture is governed by interphase properties. However, the fracture type was seen in all electrolytes independent of the interphase, and the extent of fracture correlated well with microstructure heterogeneity. These local cracks are filled with electrochemically active Li metal. The active Li metal in the cracks can be cycled and thus contribute to localized stress within the solid electrolyte, which accumulates and ultimately leads to catastrophic failure by fracture.

RESULTS AND DISCUSSION

We investigated a series of thiophosphate solid electrolytes with varying microstructures and interphase properties (A-LPS, LPS:0.5Lil, Lil-AT, and Lil-AN) to assess the impact on mechanical failure (Figure 1C). Mechanical failure in thiophosphate solid electrolyte manifests as cracks that traverse through the bulk of the material (Figure 1B). Crack propagation through the bulk is spatially non-uniform in terms of density and morphology. The material properties of the solid electrolyte (e.g., microstructure, density, interphase structure) can influence fracture events. A-LPS is an amorphous sulfide glass-ceramic

Matter Article



electrolyte (Li₃PS₄) that is kinetically unstable and can form a lithiated interphase composed of Li₂S and Li₃P by-products. An interphase can lead to an increase in cell polarization with cycling and cell failure. Extensive interfacial decomposition of A-LPS upon contact with metallic Li is observed from tomography experiments and is evidence of an unstable interphase (Figures S1A and S1B). Solid electrolytes with kinetically metastable interphases can be obtained by doping LPS with Lil. Lil addition leads to higher mobile Li⁺ concentration as well as interfacial decomposition to ionically conducting Lil along with the typical LPS decomposition products (Li₂S and Li₃P). Thus, the ion-conducting interphase coupled with better Li wettability contributes to better anode stability in the iodine-doped LPS (LPS:0.5Lil). 19,29,30 To systematically change the microstructure of LPS:0.5Lil, two different postprocessing techniques were utilized. First, the LPS:0.5Li solid electrolyte was milled in order to reduce the primary particle size and improve the packing density (Lil-AT). Subsequently, the milled powders were annealed, which resulted in a nanocrystalline phase with higher densification and lower porosity (Lil-AN). All samples studied (A-LPS, LPS:0.5Lil, Lil-AT, and Lil-AN) show the formation of Li_3PS_4 through the presence of the PS_4 structural unit at 420 cm⁻¹ (Figure S2A). The lack of a diffraction peaks beyond small remnant reactant reflection (Figure S2B) is characteristic of an amorphous solid electrolyte. Lil addition induces some crystallinity in the samples. A-LPS material shows a porous structure with pore sizes $>3-5 \mu m$ (Figure S3). LPS:0.5Lil, Lil-AT, and Lil-AN show consistently decreasing porosity and pore sizes (Figure S3). Energy-dispersive X-ray spectroscopy (EDS) mapping of pellets reveals a uniform iodine distribution on all doped samples (Figure S4).

The room-temperature ionic conductivity increases as A-LPS < Lil-AT < LPS:0.5Lil < Lil-AN (Figure 1D, 4.26×10^{-4} , 5.01×10^{-4} , 8.79×10^{-4} , and 2.40×10^{-3} S cm⁻¹). The corresponding activation energies for the materials are 0.111, 0.144, 0.147, and 0.148 eV for Lil-AN, LPS:0.5Lil, Lil-AT, and A-LPS. Lil-AN shows almost a 5-fold increase in ionic conductivity and a 25% reduction in the activation energies compared with the amorphous material. Long-range order as well as the particle-particle adhesion in the material is improved in a dense matrix, leading to improved ion transport properties. Reduction of ion-blocking pores can also contribute to improved ion transport properties (low tortuosity), and iodine doping increases the concentration of mobile Li⁺ ions and reduces interactions with the glass network, leading to improved ionic conductivity.

The electrochemical response of all the investigated materials clearly shows a decrease in polarization beyond the critical current density (CCD), with A-LPS showing an almost zero polarization. The electrochemical response is consistent with the formation of dendrites as reported previously. ^{18,66} No other mechanism was apparent with the short-circuiting cells. The CCD and cumulative charge passed before failure (charge-to-failure) follows a trend similar to that of the ionic conductivity (Figure 1E), with Lil-AN showing a maximum CCD of 4 mA cm⁻² (135.72 C cm⁻²) and A-LPS showing the minimum CCD of 0.75 mA cm⁻² (6.849 C cm⁻²). Lil-AT fails at 1.25 mA cm⁻² (19.62 C cm⁻²) and LPS:0.5Lil fails at 1.75 mA cm⁻² (41.67 C cm⁻²). Halogen-doped solid electrolytes (LPS:0.5Lil, Lil-AT, and Lil-AN) demonstrate an increased CCD compared with the undoped solid electrolyte (e.g., A-LPS). Considering current limit diagrams based on nucleation theory, the CCD is given as⁶⁷

$$j^* = \frac{(2\gamma\Omega_{\mathrm{Li}}/r_{\mathrm{c}}) + \sigma_{\mathrm{F}}\Omega_{\mathrm{Li}}}{fd(1-\alpha)|\mathbf{e}|} \cdot \frac{1}{\rho}, \tag{Equation 1}$$

where j^* is the CCD, γ is the specific energy of the interface, $\Omega_{\rm Li}$ is the volume per Li atom in the electrolyte, $r_{\rm c}$ is the critical radius, $\sigma_{\rm F}$ is the fracture stress, f is the contribution of grain boundary resistivity, d is the grain (particle/feature) size, α is the ratio





of grain boundary to grain (void/particle) size, e is the charge on the electron, and ρ is the overall resistivity. The CCD formulation arises from electro-chemomechanical potential of Li that can develop from high local resistivity or from physical irregularities in the shape of the Li interface. The model assumes a back stress that opposes the propagation of the dendrite and is considered as the fracture strength of the electrolyte material. It should be noted that while this model proposes a nucleation-controlled fracture propagation model, other mechanisms for fracture propagation also exist. Chiefly a toughness-limited fracture propagation model is also applicable to the system under study. There is an underlying uncertainty regarding the fracture propagation mechanism. However, the model can be utilized for the purpose of qualitative comparison of factors influencing CCD for the studied materials. The CCD (j*) is proportional to the ionic conductivity and inversely proportional to the total resistivity. Highly dense Lil-AN with higher ionic conductivity shows improved CCD as well as charge to failure over the other halogencontaining materials (LiI-AT and LPS:0.5Lil). Increased particle surface area in the Lil-AT material compared with the LPS:0.5Lil material can lead to a higher effective grain boundary resistance for the milled material. This results in a lower ionic conductivity and CCD for Lil-AT compared with LPS:0.5Lil. Lil-AN shows the highest CCD due to the higher ionic conductivity, higher charge carrier concentration due to halide doping, and lower grain boundary resistance due to improved density.⁶⁸ Interfacial effects of halogen doping can also aid in improving the CCD. Uniform contact between the plating/stripping surface of the Li metal anode and the electrolyte leads to planar Li plating and stripping. Iodine can potentially act as a protective layer to ensure a congruent, contiguous interface between LPS and Li metal while also preventing the continuous decomposition of LPS in contact with Li metal.

A nanoscale understanding of interphase compositional and morphological transformations during electrochemical cycling is challenging because there are limited nondestructive techniques capable of probing local dynamics at these local interfaces. In situ TEM (Figures 2 and S5) was implemented to assess the chemomechanical response of the solid electrolyte during Li stripping and plating. The solid electrolyte was benchmarked with ex situ experiments described in Supplemental Information to ensure solid electrolyte stability for in situ studies. Li metal was placed on a metal probe while the solid electrolyte (Lil-AN) was mounted on a Cu TEM half-grid (Figures 2A-2C). Lil-AN and Li metal are imaged prior to contact (Figure 2D), on physical contact (Figure 2E), electrochemical reduction (Figure 2F), and electrochemical oxidation (Figure 2G), and after probe retraction (Figures 2H and 2I). When a reducing bias is applied to Lil-AN, Li⁺ ions are drawn out of the solid electrolyte (Lil-AN) and deposited on the Li probe. A void or pore forms in the solid electrolyte region in contact with the metallic probe after electrodeposition and is highlighted with a green box in Figure 2F. This void is irreversible and remains after oxidation (Li⁰ is stripped from the probe) (Figure 2G). The interphase void formation or loss of mass is evidence of edge chipping. Edge chipping is a fracture mode that most prominently occurs due to concentrated loads⁶⁹ or from a sharp contact. ⁷⁰ While the probe can be considered a sharp contact, there was no edge chipping observed upon initial contact (Figure 2D). Pore formation and/or edge chipping only occurred after electrochemical reduction of the solid electrolyte (Figure 2F). This early-stage fracture mode, observed within the interphase, is likely due to chemomechanical driving forces.³⁹ Local stresses within a solid electrolyte can affect dissolution and deposition kinetics (Li⁰ dissolution Li⁺) and ionic transport pathways^{36,71} and can lead to local "hotspots" for ionic flux. 72,73 This ionic flux directionality is postulated to be equivalent to an ionic concentrated load at solid|solid interface and be the origin for the observed edge chipping.





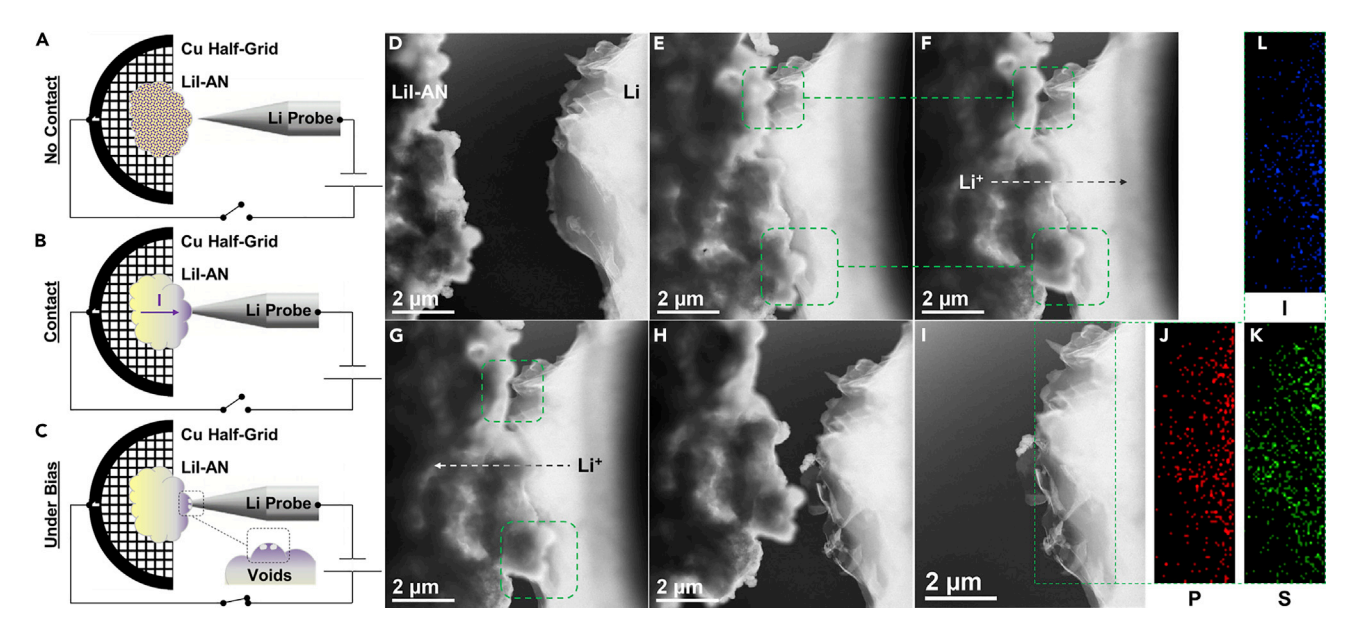


Figure 2. Interphase Transformation Tracked by In Situ TEM

- (A) Animation of the in situ TEM Nanomanipulator holder highlighting the arrangement of Li and Lil-AN.
- (B) Animation depicting the contact of Li and Lil-AN and resulting chemical processes (migration of iodine) within the TEM.
- (C) Animation depicting the electrochemical processes (formation of voids) observed upon application of bias within the TEM.
- (D) HAADF-STEM image of the Li probe and Lil-AN solid electrolyte prior to contact.
- (E) HAADF-STEM image of the Li probe and Lil-AN upon contact highlighting regions of interest for the purpose of this study.
- (F) HAADF-STEM image of variations in the highlighted sections via appearance of voids along the Li/Lil-AN interface after plating of Li.
- (G) HAADF-STEM image after the stripping of Li with the retention of formed voids during Li plating in the highlighted sections.
- (H) HAADF-STEM image of the detached Li probe and Lil-AN after a Li plating/stripping cycle.
- (I) HAADF-STEM image highlighting an area of interest on Li utilized for EDS mapping after Li plating/stripping experiments.
- (J-L) (J) Phosphorus, (K) sulfur, and (L) iodine EDS maps of the highlighted area in (I).

See also Figure S5.

High-angle annular dark-field scanning TEM (HAADF-STEM) images and EDS maps of the solid electrolyte after cycling show a uniform distribution of iodine, phosphorus, and sulfur across the entire imaged area (Figure S5). After electrochemical plating (Figure 2F) and stripping (Figure 2G) of Li⁰, the presence of iodine remains evident in the Li metal (Figure 2L). Iodine diffusion to the solid electrolytellithium metal interface is observed under both equilibrium (quiescent) and electrochemical biasing conditions. Iodine diffusion occurs at the point of contact between the solid electrolyte and metallic Li and readily diffuses away from the point of physical contact (Figure 2L). This indicates that iodine diffuses along the entire Li metal surface and is not restricted to the region of physical contact. Surface diffusion of iodine provides a uniform deposition surface for Li metal during cycling. A uniform interface reduces the cell impedance and results in a reversibly smooth overpotential response. The intimate contact afforded by an iodine-rich interface between Li metal and the solid electrolyte can enable efficient ion transport through the interphase and lead to improved electrochemical performance.

In situ synchrotron XCT was carried out on all mentioned LPS-based materials to quantitatively assess the onset and growth of mechanical failure and observe subsurface material transformation pathways upon Li cycling. It should be noted that the sample pellets (~2 mm) were slightly larger than the field of view (1.8 mm) of the tomography setup, and consequently the imaged region is from the center of the pellet. Symmetric Li-SE-Li cells were assembled in the *in situ* cell⁴³ to observe



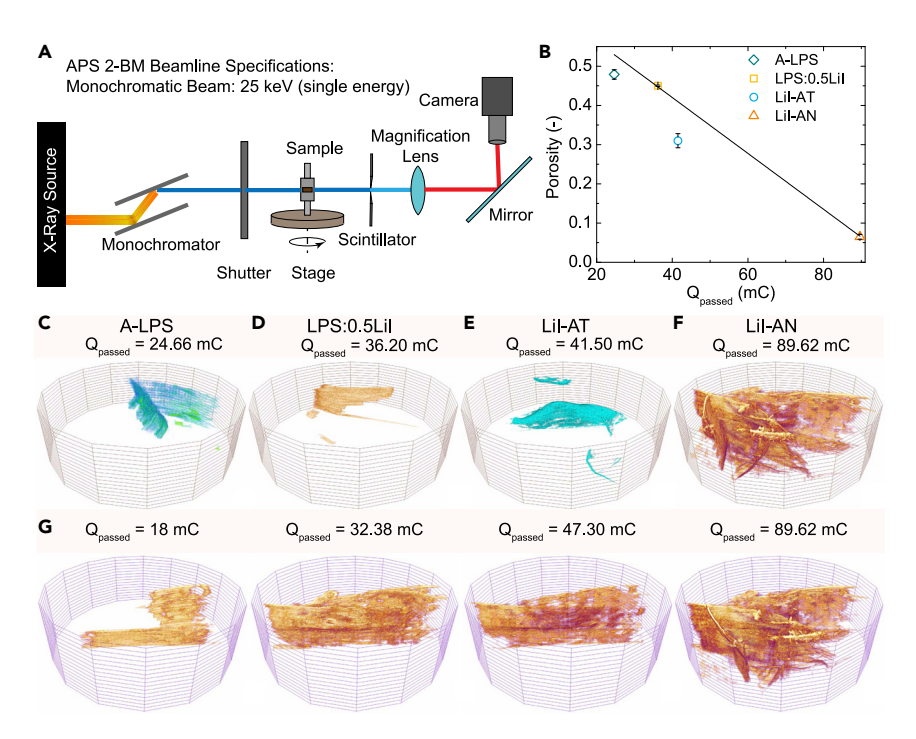


Figure 3. Failure Onset and Growth Tracked by In Situ Synchrotron Tomography

(A) Schematic diagram of the tomography setup used for in situ imaging of solid electrolytes.

(B) Correlation between the porosity measured from the tomography experiments and charge to failure.

(C-F) 3D representation of cracks of the failed samples after cycling for (C) A-LPS, (D) LPS:0.5Lil, (E) Lil-AT, and (F) Lil-AN.

(G) Crack propagation through Lil-AN sample at various plating and stripping steps.

The colors in (C) to (G) are only used to aid visualization. See also Figures S6–S9.

plating and stripping behaviors at 0.5 and 1 mA cm⁻² (Figure 3A). The in situ cell shows a higher overpotential for Li plating and stripping than the conventional coin cell due to the low applied pressure (≤ 0.5 MPa) (Figure S6). All the cells were run at increasingly higher current densities until either the polarization reduced to zero or the overpotential value exceeded the range of the potentiostat. The shorting of the in situ cell was confirmed by electrochemical impedance spectroscopy (Figure S7). The sample porosity before electrochemical cycling, computed from the reconstructed three-dimensional (3D) images, range from 0.48 for A-LPS sample to \approx 0.05 for Lil-AN sample (Figure 3B). It should be noted that the resolution of the tomography technique employed is 0.7 µm. Pores smaller than this size are not resolved and may lead to an underestimation of the porosity values. The chargeto-failure values for in situ experiments follow the trend A-LPS < LPS:0.5Lil < Lil-AT < Lil-AN (25, 35, 40, and 90 mC). The outer bounds of the trends are consistent between the lab-scale experiments and the synchrotron experiments. However, the LPS:0.5Lil and Lil-AT show different trends, with the latter showing a slightly higher charge-to-failure for the synchrotron experiments. The variation between the samples is small (≈5 mC) and could arise from small differences in assembly in the in situ cell. All materials were stable during the course of the in situ experiment and did not show signatures of material degradation (Figure S1). Inherent instability of LPS with Li metal can lead to interphase formation that manifests as material transformations (volume change, cracking, and increase in porosity). Thus, the observed material transformations are largely driven by electrochemistry rather than chemical decomposition.





XCT works primarily on the principle of absorption contrast, whereby the intensity of a beam traversing through the sample is attenuated according to the Beer-Lambert law,

$$I = I_0 \exp(-\mu(x)x), \qquad \text{(Equation 2)}$$

where I is the intensity of the transmitted beam, I_0 is the incident beam intensity, and $\mu(x)$ is the absorption coefficient of the material. Denser materials characterized by high-Z elements (solid electrolyte) attenuate the X-rays more than low-Z elements (Li metal and/or air). This difference in attenuation allows for tracking individual material transformations during electrochemical cycling. As the raw reconstructions show (Figure S8), there are distinct features with significantly lower grayscale value compared with the bulk solid electrolyte grayscale value observed in the pristine sample. The darker regions highlighted are thus identified as cracks/dendrites, as this value corresponds to a less dense phase than LPS. The fracture regions were segmented out from the raw reconstruction images for visualization (Figures 3C-3F). The segmentation was carried using consistent semi-automated procedures for all the samples. Due to the small feature size of the fracture event and segmentation methodology, the crack regions are generally overestimated (rather than underestimated). However, since the segmentation protocol is consistent at all steps and across samples, comparisons can be made between them. The cracks are concentrated in one region of the pellet for A-LPS, LPS:0.5Lil, and Lil-AT, while the crack is uniformly distributed in the Lil-AN samples. The fracture region grows toward regions with high porosity during symmetrical cycling, which mimics a Griffith crack-like mechanism. 15 The overall mechanical strength of the solid electrolyte in regions with high porosity will be low and be more susceptible to fracture. All solid electrolytes have some level of meso- and microstructure that is introduced during materials processing. Although it is ideal to have a low-porosity material, the way the material is pressed in a pellet can lead to non-uniform pore sizes throughout the pellet. Regions with high porosity contribute to tortuous ion transport that can locally magnify the current density and electric fields. The latter effect may promote localized ionic flux capable of chipping the solid electrolyte interface.

The cracks were also segmented at the end of individual charging/discharging steps to visualize the onset and growth mechanism of crack propagation of the sample (Figures 3G and S9). Based on these images, it was found that all the materials showed two distinct failure modes (Figure 4A): (1) edge-chipping failure at the electrodelelectrolyte interface and (2) vertical crack growth through sample thickness originating from the edge-chip. The fracture onset via edge chipping is likely due to directed ion transport (chemomechanics) in the interphase as seen with in situ TEM experiments (Figure 2F). Interphase void generation leads to regions of high current density and stress concentration that can lead to fracture of the solid electrolyte at the interface. Stress generation at the interphase typically arise from electrodeposition and electrodissolution of Li metal. These processes are generally coupled with large volume changes that impart stress on the solid electrolyte. Interphase void generation mechanism is consistent over length scales and is effectively observed as the crackonset mechanism. In situ tomography corroborates microscopy observations and demonstrates initiation of edge chipping at the stripping electrode (Figures 4B and 4C). Subsequently, from this region a lateral crack develops that grows through the thickness of the sample (Figure 4D). Similar interface-driven fracture was proposed previously for sodium β -alumina solid electrolytes.⁷⁴ Surface irregularities were identified as potential stress concentration regions through which fracture can initiate. Metal flow through this surface-driven crack propagates the fracture through the thickness of the electrolyte leading to ultimate failure by shorting. Edge-chipping failure mode is characterized by removal of material from a surface/



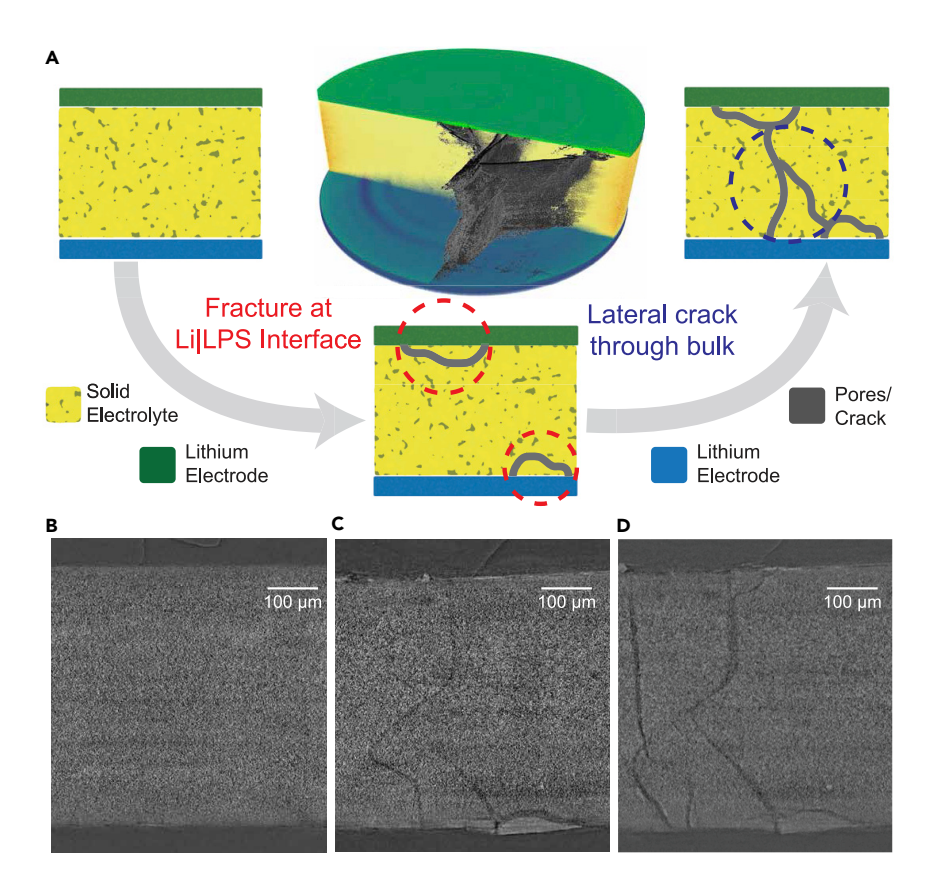


Figure 4. Fracture Growth Mechanisms in Thiophosphate Solid Electrolytes

(A) Schematic diagram showcasing the failure onset and growth mechanism in LPS solid electrolytes. Pristine LPS pellet shows a heterogeneous distribution of porosity (darker regions). Mechanical failure initiates by chipping failure of an electrolyte block at the electrode|electrolyte interface. The chipping mechanism is initiated by active electrochemical oxidation and reduction and is not observed on passive contact. Further cycling leads to lateral crack growth from the regions showing chipping failure through the thickness of the electrolyte.

(B-D) Sectional reconstruction images of Lil-AN material clearly show these distinct phenomenological mechanisms: (B) pristine, (C) chipping failure, and (D) lateral crack growth. See also Figure \$10.

edge section due to high stress concentrations and is widely observed in material shaping, tribology, anthropology, and dentistry. ^{70,75–78} The edge chipping was observed in all thiophosphate electrolytes (independent of microstructure) and is likely chemomechanically driven. The through-plane or vertical fracture is a result of the solid electrolyte microstructure.

All samples showed an identical fracture initiation and propagation mechanism despite differences in microstructure and interphase properties (Figure 4). These results indicate that while halide doping can kinetically stabilize the Li metal-LPS interface, the eventual failure mechanism for all the samples is identical and independent of the interphase composition. Edge-chipping is observed at both electrodes, and the short happens when the propagating lateral cracks merge within the bulk. Li metal penetration into the fracture is also observed over cycling and ultimately increases the total SE surface area in contact with lithium metal. Solid electrolyte in contact with Li within these crack features can undergo interphase formation and related chemomechanical transformations as evidenced from TEM measurements. Additional interphase formation within the cracks can lead to an





accelerated failure. TEM and X-ray microscopy offer complementary insight into the mechanistic origin of failure within the material at cascading length scales, which is vital to obtaining a complete understanding of the failure process. Specifically, the TEM results highlight differences in Li plating/stripping mechanisms with an electrochemically driven surface pitting reaction of the LPS material with Li metal. At the macroscale, XCT identifies an "interface chipping" mechanism as the mode through which all the investigated samples initiate failure. This mechanism is likely the manifestation of the interfacial pitting mechanism observed with the *in situ* TEM. In this way, TEM provides needed nanoscale interfacial chemistry information and XCT serves to complement it by examining real pelletized samples so that we can observe the individual failure mechanisms from each technique as well as how these mechanisms cascade into each other. Combining tomography and TEM provides unique collective insight into the failure-onset mechanism in LPS electrolytes over several length scales.

In situ TEM revealed that iodine rapidly diffuses to the solid electrolyte|Li metal interface. This will result in a compositional gradient in the solid electrolyte. Prior work demonstrated that halide doping led to materials with lower Young's modulus and less elasticity due to a larger free volume. 49,79 Thus, iodine diffusion to the interface will lead to non-uniform mechanical properties throughout the solid electrolyte. Solid electrolytes doped with a halogen will have electrode-electrolyte interfaces with lower Young's modulus compared with the bulk. These interfaces will be more compliant and will better accommodate the stresses associated with electrodeposition and electrodissolution of Li, and maintain a conformal interface between the SE and Li. This can lead to the higher CCD and charge-to-failure measured for the halogen-doped solid electrolytes. Iodine doping and improved packing density of annealed samples result in higher performance metrics (CCD, Q_{failure}). While the failure-onset mechanism is identical for all LPS materials, the extent of crack propagation (density of cracks in the bulk) varies significantly between the different materials. This suggests that the lateral crack growth is governed by differences in bulk pellet microstructure.

Solid electrolyte microstructure heterogeneity can result in non-uniform mechanical stress. Regions with higher porosity have lower yield strength, which results in larger deformation and damage in these regions. Thus, lateral crack growth tends to nucleate at porous regions (Figures S9 and S10). Microstructure variability can be quantitatively assessed with a porosity factor (Figures 5A and 5B). Porosity factor is defined as the variation in local porosity compared with the mean porosity:

$$d = \frac{\Phi}{\Phi_0} - 1,$$
 (Equation 3)

where d is the porosity factor, Φ is the local porosity, and Φ_0 is the mean porosity calculated on a binarized dataset. Porosity maps are calculated across two normal planes in the electrolyte defined as through-plane and in-plane directions (Figure 5B). In-plane sections are normal to the applied electric field and represent the horizontal cross-section of the pellet. Through-plane is parallel to the applied electric field and represents the vertical cross-section of the pellet. Mapping the porosity factor along the through-plane direction, we clearly observe local regions with inhomogeneous microstructure compared with the average microstructure (Figures 5C–5F). A-LPS shows a more homogeneous distribution of porosity factor compared with Lil-AN, which has a highly inhomogeneous distribution through the section. Porosity factors mapped here are local measurements that reflect the microstructural features at specific locations in the sample. It should be noted that



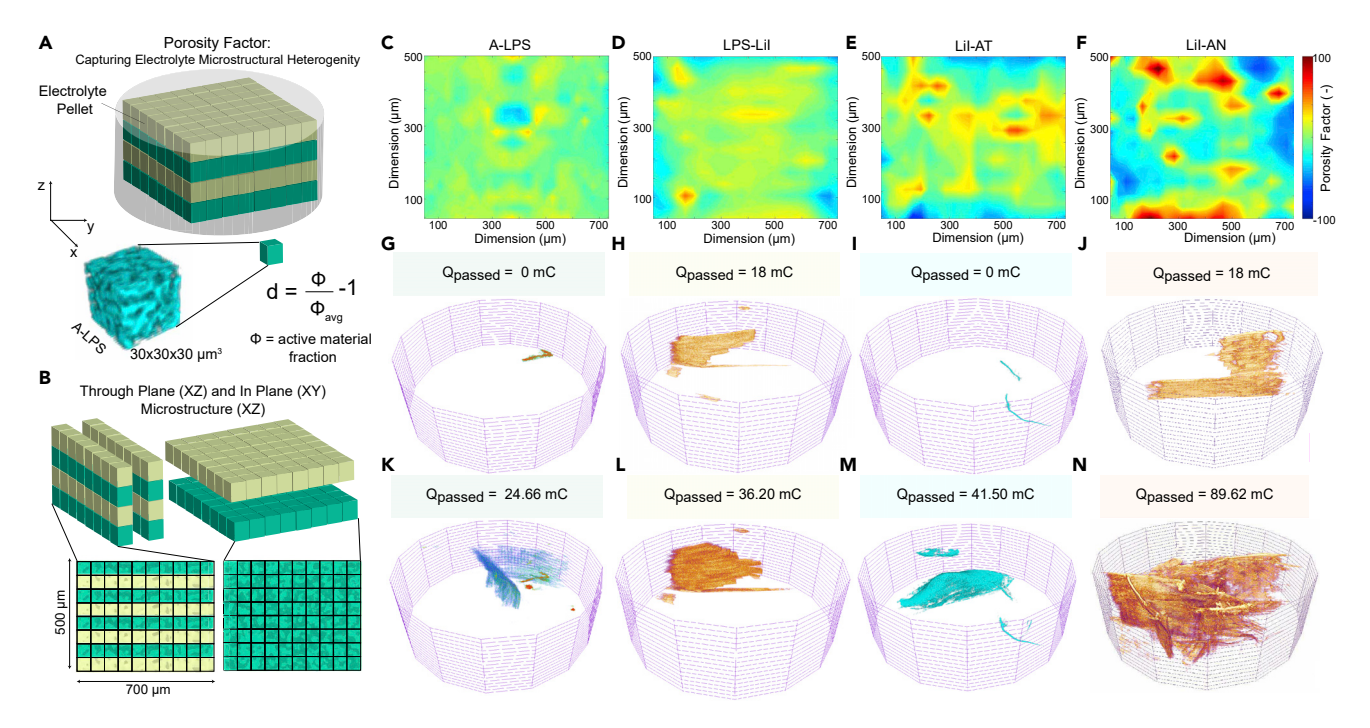


Figure 5. Assessing Microstructural Heterogeneity in Solid Electrolytes by Porosity Factor

(A) Electrolyte pellet is discretized into uniform subvolumes of 30 \times 30 \times 30 μ m³ dimension.

(B) Porosity factor is defined as the ratio of local porosity identified for the 30 \times 30 \times 30 μm^3 subvolume to the average porosity of the pellet. Microstructure of a representative subvolume of A-LPS pellet is shown.

(C–N) Porosity maps are calculated across two normal planes in the electrolyte defined as through-plane and in-plane directions. In-plane sections are normal to the applied electric field and represent the horizontal cross-section of the pellet. Through-plane is parallel to the applied electric field and represents the vertical cross-section of the pellet. Porosity factor variation in through-plane direction for (C) A-LPS, (D) LPS:0.5LiI, (E) LiI-AT, and (F) LiI-AN. Initial crack formation in samples for (G) A-LPS, (H) LPS:0.5LiI, (I) LiI-AT, and (J) LiI-AN. A-LPS and LiI-AT pristine pellets showed regions with microstructure distinct from the average microstructure. Hence, those morphologies are visualized. 3D representation of cracks of the failed samples after cycling for (K) A-LPS, (L) LPS:0.5LiI, (M) LiI-AT, and (N) LiI-AN.

See also Figures \$11-\$13.

the porosity factor shown here is a relative change in the local microstructural property compared with a mean microstructural property. Statistically, the absolute variation of local porosity should be identical because all pellets are processed in a similar way. Normalizing this value by the mean porosity gives an insight into the degree of structural heterogeneity. For A-LPS sample, with a mean porosity of 0.48, a local variation of 0.02-0.03 does not deviate significantly from the average microstructure. However, for Lil-AN, a local variation of 0.02-0.03 is comparable with its mean porosity (0.05), which is characterized as high structural heterogeneity (Figures 5C-5F). Statistical analysis of porosity factor was carried out on 40 distinct \approx 750 x 500×30 -µm³ electrolyte cross-sections (Figure S11). Statistical assessment of the porosity factor across this dataset shows consistent results with A-LPS showing a homogeneous, narrow distribution of porosity factor while Lil-AN shows a more heterogeneous, wide distribution of porosity factors. This is further verified by in-plane assessment of porosity factor across different subvolume sizes for the raw grayscale dataset to remove errors from the binarization process (Figures S12 and S13). These studies also show consistent results, with Lil-AN having the most heterogeneous microstructure (compared with its mean value). The influence of porosity factor distribution is observed on the crack formation within the electrolytes (Figures 5G-5N). A-LPS, which showed a relatively homogeneous porosity factor, shows focused crack formation in the vicinity of a microstructural feature present in the pristine sample (Figures 5G and 5K). In comparison, Lil-AN, which shows highly heterogeneous

Matter Article



porosity factor distribution, shows extensive crack propagation through the entire bulk of the sample with no apparent focused crack growth (Figures 5J and 5N). LPS:0.5Lil and Lil-AT show similar behavior in terms of crack formation and porosity factor distribution. Crack growth through the sample is dictated by the mechanics of the bulk electrolyte. The microstructural variation observed in the pellets indicates that cracks will preferentially grow through the regions with higher porosity (lower porosity factor) due to the reduced local yield strength and fracture strength. Additionally, higher porosity increases the local tortuosity in the region, leading to an enhanced current density and electric field in the vicinity. These effects lead to crack formation in regions with high microstructural heterogeneity. It should be noted that for a Griffith-type approach, larger (raw) defect size and volume fraction of the porosity are critical factors dictating fracture growth. 80-83 Porosity factor is a measure of variation of the local microstructure from the average pellet microstructure. In this regard, a variation in the porosity factor (structural heterogeneity) will occur when the local domains show either a higher density of pores (volume fraction) or larger pore sizes. Thus, both interpretations (porosity factor/Griffith mechanism) are analogous and identify the same mechanism for fracture. Controlling porosity and pore distribution within the pellet will be important to tailor solid electrolytes for high rate capability.

Current focusing can occur because of solid electrolyte microstructure heterogeneity or constriction effects. Constriction effects can lead to polarization and are often due to distant active microcontacts (irregular contact), which lead to lower contact surface area, local regions with higher current densities, and high stress distributions. 84,85 These non-conformal regions can accelerate material transformations, leading to failure. To effectively rule out that sample contact had a role in current focusing, we created interfacial intensity maps (Figure 6) similar to those reported earlier. 85 Interfacial intensity maps qualitatively indicate the degree of interfacial contact and are generated by normalizing the grayscale intensity of a 150 x 150μm² section at both Li-SE interfaces over at least a 500-μm thickness for the pristine cell (Figure 6A). Regions with high normalized intensity signify high-attenuation materials (solid electrolyte) while lower-intensity materials signify transparent regions (air/voids). The resolution of this map is identical to the tomography resolution of $0.7 \mu m$. Interface is generally estimated where a sharp change in intensity is observed in the two-dimensional map corresponding to the step from Li (low intensity) to the solid electrolyte (high intensity). Some gradient exists within the high-intensity region for A-LPS compared with the other electrolytes, which reflects the porosity of the amorphous LPS material. The jump region (interface) is fairly sharp and similar for all the materials (Figures 6B, 6C, and \$14) such that qualitatively they can be considered identical. More so, no regions of very low intensity are observed, indicating that the SE-Li interfaces are identical for the tested materials. The identification of heterogeneity at the interface is limited by the size of the voids, resolution of the technique, and the contrast available between Li and void regions. For the given experimental conditions, no discernible differences are observed in the average interface conformation for the four samples. This indicates that the crack-formation mechanisms are driven by inherent material microstructural heterogeneity and not by variations in cell assembly (contact between electrode and electrolyte).

Resolving Li filaments in the bulk solid electrolyte is a challenge because both voids and Li have low contrast and will be transparent. Thus, instead of directly tracking Li filament within the bulk electrolyte, we indirectly monitor it by tracking the total transparent region. An increase in the transparent region will occur either via an





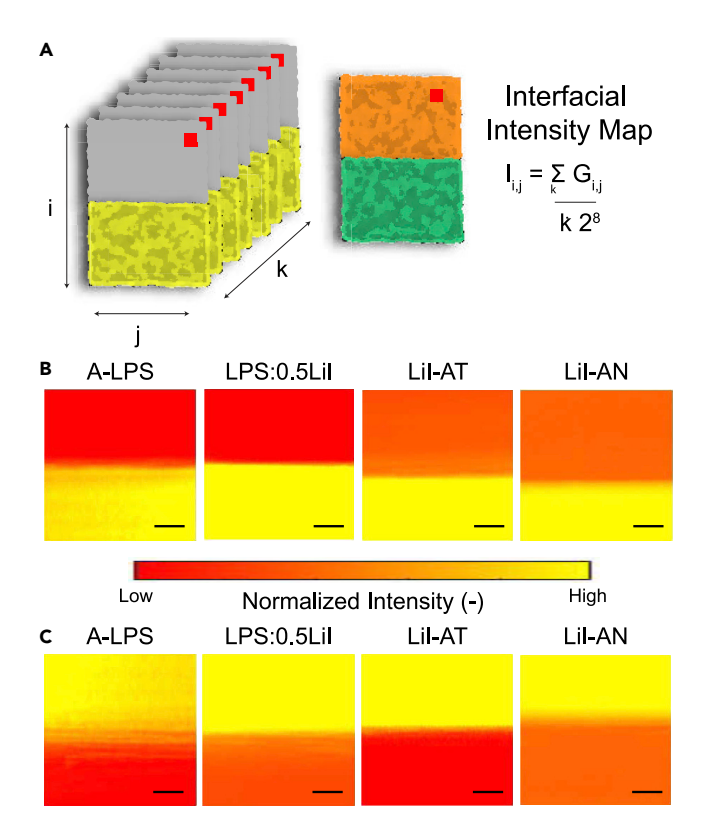


Figure 6. Interfacial Intensity Map at the Solid-Solid Interface

(A) Schematic diagram explaining the measurement of intensity maps. Raw grayscale intensity is traced a 150 \times 150- μ m² section over at least 500- μ m depth. This is normalized to the depth and the maximum theoretical intensity of an 8-bit image. The resultant image provides insight into the density variation and presence of pores/voids within the imaged section. (B and C) Intensity map for the top Li-SE interface is shown in (B) while the bottom SE-Li interface is shown in (C). Scale bars, 30 μ m.

increase in the void region (via fracture growth) or by the presence of Li metal in the bulk solid electrolyte. X-ray transparent region volume within the solid electrolyte bulk is tracked during cycling to assess the presence of electrochemically active material within the LiI-AN solid electrolyte (Figure 7A) and A-LPS,LPS:0.5LiI, and LiI-AT (Figure S15). The X-ray transparent region volume grows at crack onset and oscillates on subsequent cycles (Figures 7C and S15) prior to failure by shorting for all the samples studied. It should be noted that the absolute crack volumes are most likely overestimated due to segmentation challenges. However, the trends between individual steps can be compared, as the same segmentation protocols were employed across all the samples. The X-ray transparent regions are areas showing lower absorption than the surrounding electrolyte material, which can be pores, cracks, or Li metal, all of which have low absorption coefficients. The volume modulation of the X-ray transparent region can be presence of electrochemically active material (Li) within the cracks (Figure 7B). Presence of metal in crack is consistent with the failure mechanisms proposed for other solid electrolytes.⁷⁴ During the plating cycle, Li can be deposited in the crack onto a filament growth or be deposited in an isolated form. ⁴² On stripping, if this material is electrochemically accessible it will be oxidized and shuttled to the other electrode. Preferential plating and stripping from the filament lead to stress generation owing to material addition and removal from within a confined space (Figure S16). If the extensive stress from the dendrite growth

See Figure S14.





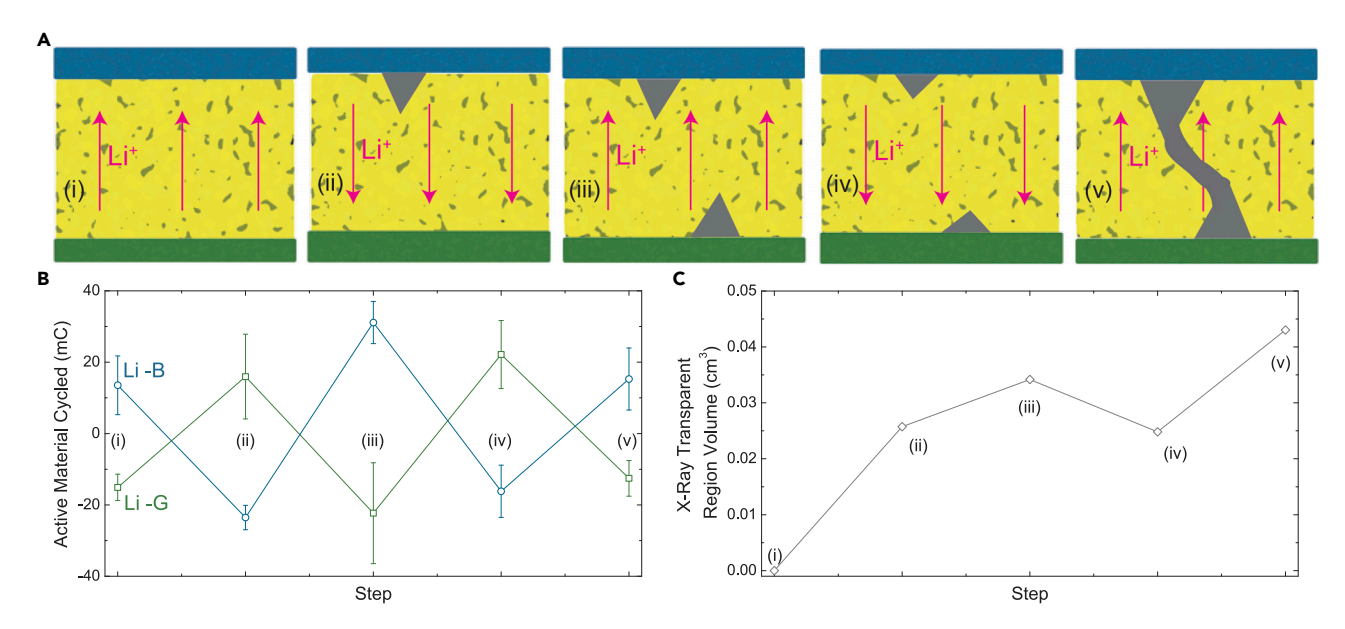


Figure 7. Crack Volume Modulation on Cycling in Lil-AN

- (A) Schematic diagram representing the variation in imaged crack volume upon cycling.
- (B) Difference in average electrode thickness of the plating and stripping electrode as a function of cycle steps. Li-B represents the top blue electrode, and Li-G represents the bottom greeen electrode in part (a).
- (C) Absolute crack volumes measured as a function of cycle steps.

See also Figures S15 and S16.

supersedes the restoring force offered by the fracture strength of the material, it can lead to propagation of fracture. Li filament growth into the solid electrolyte also increases the Li|LPS interfacial area. The regions with new interfacial contact between Li and solid electrolyte undergo interphase formation and chemomechanical transformations such as void formations, iodine migration, and stress gradient formation as evidenced from the *in situ* TEM measurements.

A validation of Li filament growth within the imaged cracks is carried out by assessing the cycled capacity from the individual electrodes of the symmetric cell at each step (Figures 7B and S15). The cycled capacities are estimated from the change in thickness of the electrode between successive plating/stripping steps. The thicknesses of the electrodes are averaged over 15 spatial locations across the sample, assuming planar plating and stripping. While this assumption is not very accurate, it provides some information regarding the depth of discharge from individual electrodes. We clearly observe an unequal amount of plated and stripped charge for the individual electrode, especially for later steps. The excess charge can be thought to reside in the X-ray transparent regions imaged and thus account for the modulation of the crack volumes observed. Non-uniform crack formation and subsequent fatigue loading by cycling of active material through the cracks can lead to fracture of the solid electrolyte.

Conclusions

In summary, the effect of interfacial chemistry and microstructure on the mechanical failure of LPS-based solid electrolytes was investigated using advanced multimodal characterization techniques. Kinetically stable interphase and microstructural control is engineered by iodine doping, and milling and annealing. The annealed samples with iodine doping show the highest room-temperature conductivity of





 $2.4 \times 10^{-3} \,\mathrm{S\,cm^{-1}}$ and CCD of 4 mA cm⁻². In situ TEM results show iodine migration to the Li metal surface and void formation at the LPS interface on electrochemical cycling. Void formation only occurs upon electrochemical cycling, which suggests that the transformation is chemomechanically driven via local "hotspots" in ion flux. Iodine migration to the Li metal surface affords nanometer-scale intimate contact with Li metal, resulting in improved electrochemical performance of the Lilcontaining materials. Void formation at the LPS interface is an inherent material response to electrochemical cycling and is not observed on passive contact. Material transformations during cycling are evaluated using in situ synchrotron XCT. A consistent failure mechanism across all materials is identified by tracking evolution of the crack features with in situ tomography. Mechanical failure is initiated with edge cracking at the interface and subsequent lateral crack growth through the surface. The onset of failure at the Li|LPS interface is consistent with the void formation observed in the TEM studies. Extent of crack propagation within the bulk solid electrolyte is assessed by tracking the porosity factor of solid electrolytes. The annealed sample shows large spatial microstructural heterogeneity, leading to an extensive crack formation through the bulk dictated by the tortuous ion flux pathways and disparate local mechanical properties. Volume modulation of X-ray transparent region and non-symmetric depth of discharge on the two electrodes indicates Li filament growth and the presence of active material within fracture sites. Non-uniform crack formation and subsequent fatigue loading by cycling of active material through the cracks can lead to fracture of the solid electrolyte. In situ TEM and XCT corroborate the failure mechanism across cascading length scales. Multimodal characterization offers a unique insight into failure mechanisms of solid-state batteries. This work provides significant new insight into fracture onset and growth mechanisms in sulfide solid electrolytes. These results are anticipated to inform future work on processing and operation of next-generation solid-state batteries. While the decomposition product (e.g., interphase) between the solid electrolyte and electrode does affect failure, this work highlights the significance of microstructural heterogeneities on failure. Dense solid electrolytes with limited microstructure heterogeneity are imperative for the high-current-density operation of all solid-state batteries.

EXPERIMENTAL PROCEDURES

Resource Availability

Lead Contact

K.B. Hatzell serves as lead contact and is familiar with the Cell Press editorial policies.

Materials Availability

No unique reagents were generated in this study.

Data and Code Availability

All data are available from the lead contact upon reasonable request.

Sample Preparation

Synthesis of Li-3PS-4 (A-LPS)

Anhydrous lithium sulfide (Li₂S) (Aldrich, 99.98%) and anhydrous phosphorus pentasulfide (P_2S_5) (Sigma-Aldrich, 99%) first form a mixture (2.0 g total) containing a molar ratio of Li₂S/ P_2S_5 = 3:1. This mixture was ground by hand in an agate mortar/pestle for 5 min and then transferred to a 45-mL zirconium oxide (ZrO₂) ball-mill pot along with 32 g of ZrO₂ balls (5 mm diameter). The mixture was ball-milled for 40 h using a planetary ball mill (Pulverisette 7, Fritsch). Thereafter, the yellow lithium thiophosphate (Li₃PS₄, or LPS) powder was collected.

Matter Article



Synthesis of Li₃PS₄:0.5LiI (LPS:0.5LiI)

Anhydrous lithium iodide (Lil) beads (Aldrich, 99.999%) were added to an agate mortar/pestle and pulverized. Lil was then moved to a new mortar along with anhydrous Li₂S and anhydrous P₂S₅ to form a mixture (2.0 g total) containing a molar ratio of Li₂S/P₂S₅/Lil = 3:1:1. This mixture was ground for 5 min and transferred to a 45-mL ZrO₂ ball-mill pot along with 32 g of ZrO₂ balls (5 mm diameter). The mixture was ball-milled for 40 h using a planetary ball mill (Pulverisette 7, Fritsch). Each cycle consisted of spinning the pot for 1 h at 550 rpm and then resting the pot for 5 min. Thereafter, the LPS-0.5Lil (light yellow) powder was collected.

Synthesis of Attrition Milled LPS:0.5Lil (Lil-AT)

Two grams of LPS:0.5Lil was transferred to a 45-mL ZrO_2 ball-mill pot along with 43 g of ZrO_2 balls (1 mm diameter). Six grams of dried heptane was added to the pot before sealing. The mixture was ball-milled for 12 h using a planetary ball mill (Pulverisette 7, Fritsch). Each cycle consisted of spinning the pot for 1 h at 200 rpm and then resting the pot for 5 min. The white powder was collected and rinsed with 6 g of dried heptane and heated on a hotplate while stirring at 100° C for 3 h. Thereafter, the Lil-AT (white color) powder was collected.

Synthesis of Annealed LPS:0.5Lil (Lil-AN)

Two grams of Lil-AT was placed into a stainless-steel can on a hotplate. The mixture was heated at 185°C for 3 h while stirring every 20 min. Thereafter, the Lil-AN (lightgray color) powder was collected.

Materials Characterization

Raman spectroscopy was performed with a Horiba LabRAM HR spectrometer equipped with an inverted optical microscope. A $50\times$ lwr objective lens was used to focus a 532-nm laser onto the powder sample, which was pressed against the inside surface of a sealed cuvette to protect it from air. The backscattered light was dispersed using a 600 lines/mm grating onto a charge-coupled device camera. Spectra were collected from three different spots on each sample and compared with confirm sample homogeneity. X-Ray diffraction patterns were collected on a lab diffractometer for $10^{\circ} < 2\theta < 90^{\circ}$.

Cell Assembly and Electrochemistry

Fabrication of Impedance Measurement Cells

One hundred milligrams of solid electrolyte powder was added to the hole in a Macor ring (surface area [SA] = $1.0~\rm cm^2$) and cold-pressed between two steel pistons into a pellet under 4 tons of pressure for 5 min. Next, carbon-coated aluminum foil (MTI) disks were placed against both sides of the pellet and the stack was pressed again under 3 tons for about 1 min. After removing the stack from the press, the pistons were anchored in place by a cell top and bottom, held together by insulated bolts. The bolts were tightened to 2 N·m, which provides a stack pressure of about 88 MPa. Finally, the cell was sealed in an argon-filled container and placed into a temperature-controlled oven. Electrochemical impedance spectroscopy was performed using a Bio-logic VMP3 potentiostat, with a frequency range from 100 mHz to 1 MHz and a potential amplitude of 10 mV. The electrolyte resistance was determined from the electrochemical impedance spectroscopy plots by extrapolating the low-frequency, linear section of the curves down to the x axis.

Fabrication of Li/Solid Electrolyte/Li symmetric Cells

For LPS:0.5Lil measurements, 100 mg of solid electrolyte was added to the hole in a Macor ring $(SA = 1.0 \text{ cm}^2)$ and cold-pressed between two steel pistons under 4 tons





of pressure for 5 min to form a pellet. A thick Li disk (99.8%, Honjo Metal) of 10 mm diameter was then polished with a toothbrush, punched from the flattened Li using a knife punch, and placed on both sides of the pellet. The final thickness of the Li foil was 150 μm . Stainless-steel pistons were pressed against the Li to form a stack, which was then sandwiched between cell top and bottom. Finally, insulated bolts were used to compress the cell to 29 MPa before placing the cell into an argon-filled container, which was then moved from the glovebox to an oven for electrochemical testing.

Critical Current Density Test

Li metal was plated and stripped at stepwise-increased current densities using a Biologic VMP3 potentiostat. At 60° C, the current density was increased in a stepwise manner from 0.1 mA cm⁻² to 4.0 mA cm⁻² in 0.25-mA cm⁻² increments. Each current was applied using 1-h half-cycles for two cycles. The CCD was ascribed to the current at which a sharp drop in potential was witnessed mid-half-cycle.

Fabrication of Synchrotron Cells

For synchrotron experiments, 2-mm electrolyte pellets were made by compressing the samples at 4 tons cm $^{-2}$ pressure. The samples were transferred to the beamline in argon atmosphere sealed containers. Symmetric Li|Li cells were assembled in the in situ cell inside an argon atmosphere glovebox (<0.1 ppm $\rm O_2$ and $\rm H_2O$) and sealed. The in situ cell was mounted on the sample stage at the end station. Electronic impedance spectroscopy was carried out before and after the complete testing of the symmetric cell between 1 MHz and 100 mHz with an amplitude of 50 mV. Plating and stripping experiments were carried out at current densities of 0.04–1.2 mA cm $^{-2}$ for 30 min. A cutoff voltage of 10 V was kept for the tests. If the polarization exceeded this value, the current density was moved to the next step.

Tomography Studies

Synchrotron X-ray tomography studies were carried out at the 2-BM beamline of the Advanced Photon Source (Figure 3A). Filtered monochromatic X-rays of 25 keV were incident on the sample. Projections (n = 1,500) were taken evenly during a 180° sample rotation with 100-ms exposure time for each projection. An FLIR Oryx ORX-10G-51S5M camera was used with a 2× magnification objective lens. The resultant voxel size was $\approx 0.7 \,\mu\text{m}$ with a field of view of 1.4 \times 0.8 mm². Under these experimental conditions, a single tomography scan took approximately 7-10 min of acquisition time. The tomography scans were taken for the pristine and the failed sample. Additionally, tomography scans were obtained at the end of each plating and stripping cycle. It should be noted that synchrotron experiments are typically carried out on a restricted time frame and carrying out in situ experiments is a time-intensive exercise. Given these constraints, only a single in situ measurement was carried out on each material type. To rigorously analyze the imaging data, we have conducted analysis on multiple locations. Supplemental Information demonstrates much of the statistical analysis that was completed on property and image analysis. We have also created automated segmentation and reconstruction algorithms to avoid introducing human bias.

Image Reconstruction, Analysis, and Quantification

TomoPy software was used for reconstruction of the raw data⁸⁶ using the Gridrec algorithm. Wavelet-Fourier ring filter removal⁸⁷ and Paganin phase retrieval⁸⁸ methods were applied for raw image manipulation. Subsequent image processing was carried out using ImageJ⁸⁹ and MATLAB. Binarization of all the samples was carried out using identical thresholding routines available in ImageJ. The thresholding protocols were kept identical across all the analyzed tomography scans to reduce variability in the results. Subvolume optimization was carried out to estimate





geometric parameters of the system. The pore size distribution ⁹⁰ plugin was used to estimate the porosity of the samples. The details of the method used to describe porosity and pore size distribution have been reported previously. ⁶¹ Identification of cracks from the binarized data was carried out by filtering pores smaller than a specified threshold volume and subsequently by visual analysis. All quantification routines were developed and implemented in MATLAB.

Microscopy Imaging Methods

Scanning Electron Microscopy/Energy-Dispersive X-Ray Spectroscopy

Scanning electron microscopy (SEM) images were collected using a JEOL 7800 FLV microscope outfitted with an Oxford EDS system, operated at 5–20 kV for all samples. All samples were loaded into an air-free SEM holder (JEOL) within an argon atmosphere glovebox (<0.1 ppm O_2 and H_2O) and transported directly to the scanning electron microscope where they were analyzed under vacuum.

Transmission Electron Microscopy/Energy-Dispersive X-Ray Spectroscopy

HAADF-STEM images were collected using a JEOL JEM-F200 microscope operated at 200 kV. Dual silicon-drift detector EDS systems with a large solid angle (100 mm²) were utilized for enhanced microanalysis of all samples via ex situ and in situ analysis modes. Further details on ex situ and in situ TEM measurements are included in Supplemental Information.

SUPPLEMENTAL INFORMATION

Supplemental Information can be found online at https://doi.org/10.1016/j.matt. 2020.09.018.

ACKNOWLEDGMENTS

M.B.D and K.B.H. were supported by the National Science Foundation under grant no. 1847029. M.B.D. and K.B.H. acknowledge the Vanderbilt Institute of Nanoscience and Engineering for access to their shared characterization facilities. K.B.H. acknowledges support from the ECS/Toyota Young Investigator Fellowship. This research used resources of the Advanced Photon Source, a US Department of Energy (DOE) Office of Science User Facility operated for the DOE Office of Science by Argonne National Laboratory under contract no. DE-AC02-06CH11357. This work was performed in part at the Singh Center for Nanotechnology at the University of Pennsylvania, a member of the National Nanotechnology Coordinated Infrastructure (NNCI) network, which is supported by the National Science Foundation (grant NNCI-1542153). The authors gratefully acknowledge use of facilities and instrumentation supported by NSF through the University of Pennsylvania Materials Research Science and Engineering Center (DMR-1720530). J.P.H. and E.A.S. acknowledge support from the NSF-DMR-MMNP (DMR-1809398). The authors would like to thank Julio A. Rodriguez Manzo, Norman J. Salmon, and Daan Hein Alsem from Hummingbird Scientific for their guidance and support during the execution of operando TEM experiments utilizing the Nanomanipulator holder.

AUTHOR CONTRIBUTIONS

K.B.H. conceived the concept and idea. N.S. and T.S.A. synthesized the material and performed electrochemical measurements. M.B.D., N.S., T.S.A., K.B.H., and P.S. performed the synchrotron imaging experiments. M.B.D. completed the image processing and analysis from the synchrotron experiments. N.S., T.S.A., J.P.H., and E.A.S did the TEM measurements. M.J. did the SEM measurements. K.B.H. and M.B.D. wrote the manuscript. All authors contributed to revision of the manuscript.





DECLARATION OF INTERESTS

The authors declare no competing interests.

Received: July 9, 2020 Revised: August 24, 2020 Accepted: September 18, 2020 Published: October 12, 2020

REFERENCES

- Cheng, X.B., Zhao, C.Z., Yao, Y.X., Liu, H., and Zhang, Q. (2019). Recent advances in energy chemistry between solid-state electrolyte and safe lithium-metal anodes. Chem 5, 74–96.
- Hatzell, K.B., Chen, X.C., Cobb, C., Dasgupta, N.P., Dixit, M.B., Marbella, L.E., McDowell, M.T., Mukherjee, P., Verma, A., Viswanathan, V., et al. (2020). Challenges in lithium metal anodes for solid state batteries. ACS Energy Lett. 5, 922–934.
- Lau, J., DeBlock, R.H., Butts, D.M., Ashby, D.S., Choi, C.S., and Dunn, B.S. (2018). Sulfide solid electrolytes for lithium battery applications. Adv. Energy Mater. 8, 1800933.
- Ujiie, S., Hayashi, A., and Tatsumisago, M. (2013). Preparation and ionic conductivity of (100-x)(0.8Li₂S•0.2P₂S₃•xLiI glass-ceramic electrolytes. J. Solid State Electrochem. 17, 675–680
- Koerver, R., Zhang, W., De Biasi, L., Schweidler, S., Kondrakov, A.O., Kolling, S., Brezesinski, T., Hartmann, P., Zeier, W.G., and Janek, J. (2018). Chemo-mechanical expansion of lithium electrode materials-on the route to mechanically optimized all-solid-state batteries. Energy Environ. Sci. 11, 2142–2158.
- Hartmann, P., Leichtweiss, T., Busche, M.R., Schneider, M., Reich, M., Sann, J., Adelhelm, P., and Janek, J. (2013). Degradation of NASICON-type materials in contact with lithium metal: formation of mixed conducting interphases (MCI) on solid electrolytes. J. Phys. Chem. C. 117, 21064–21074.
- Wenzel, S., Randau, S., Leichtweiß, T., Weber, D.A., Sann, J., Zeier, W.G., and Janek, J. (2016). Direct observation of the interfacial instability of the fast ionic conductor Li₁₀GeP₂S₁₂ at the lithium metal anode. Chem. Mater. 28, 2400–2407.
- Wenzel, S., Weber, D.A., Leichtweiss, T., Busche, M.R., Sann, J., and Janek, J. (2016). Interphase formation and degradation of charge transfer kinetics between a lithium metal anode and highly crystalline Li₇P₃S₁₁ solid electrolyte. Solid State Ionics 286, 24–33.
- Krauskopf, K.T., Richter, F.H., Zeier, W.G., and Janek, J. (2020). Physicochemical Concepts of the Lithium Metal Anode in Solid-State Batteries. Chem. Rev. 120, 7745–7794.
- Ma, C., Cheng, Y., Yin, K., Luo, J., Sharafi, A., Sakamoto, J., Li, J., More, K.L., Dudney, N.J., and Chi, M. (2016). Interfacial stability of Li metal-solid electrolyte elucidated via in situ electron microscopy. Nano Lett. 16, 7030– 7036.
- Han, F., Zhu, Y., He, X., Mo, Y., and Wang, C. (2016). Electrochemical stability of Li₁₀GeP₂S₁₂

- and $\text{Li}_7\text{La}_3\text{Zr}_2\text{O}_{12}$ solid electrolytes. Adv. Energy Mater. 6, 1501590.
- Wenzel, S., Sedlmaier, S.J., Dietrich, C., Zeier, W.G., and Janek, J. (2018). Interfacial reactivity and interphase growth of argyrodite solid electrolytes at lithium metal electrodes. Solid State Ionics 318, 102–112.
- Tippens, J., Miers, J.C., Afshar, A., Lewis, J.A., Cortes, F.J.Q., Qiao, H., Marchese, T.S., Di Leo, C.V., Saldana, C., et al. (2019). Visualizing chemomechanical degradation of a solid-state battery electrolyte. ACS Energy Lett. 4, 1475– 1483
- Wenzel, S., Leichtweiss, T., Krüger, D., Sann, J., and Janek, J. (2015). Interphase formation on lithium solid electrolytes - an in situ approach to study interfacial reactions by photoelectron spectroscopy. Solid State Ionics 278, 98-105.
- Porz, L., Swamy, T., Sheldon, B.W., Rettenwander, D., Frömling, T., Thaman, H.L., Berendts, S., Uecker, R., Carter, W.C., and Chiang, Y.M. (2017). Mechanism of lithium metal penetration through inorganic solid electrolytes. Adv. Energy Mater. 7, 1701003.
- Sharafi, A., Meyer, H.M., Nanda, J., Wolfenstine, J., and Sakamoto, J. (2016). Characterizing the Li-Li₇La₃Zr₂O₁₂ interface stability and kinetics as a function of temperature and current density. J. Power Sources 302, 135–139.
- Dixit, M.B., Verma, A., Zaman, W., Zhong, X., Kenesei, P., Park, J.S., et al. (2020). Synchrotron Imaging of Pore formation in Li Metal Solid State Batteries Aided by Machine Learning. ACS Applied Energy Materials. https://doi. org/10.1021/acsaem.0c02053.
- Kazyak, E., Garcia-Mendez, R., LePage, W.S., Sharafi, A., Davis, A.L., Sanchez, A.J., Chen, K.H., Haslam, C., Sakamoto, J., and Dasgupta, N.P. (2020). Li penetration in ceramic solid electrolytes: operando microscopy analysis of morphology, propagation, and reversibility. Matter 2, 1025–1048.
- Han, F., Yue, J., Zhu, X., and Wang, C. (2018). Suppressing Li dendrite formation in Li₂S-P₂S₅ solid electrolyte by Lil incorporation. Adv. Energy Mater. 8, 6–11.
- Atif Pervez, S., Ali Cambaz, M., Thangadurai, V., and Fichtner, M. (2019). Interface in solid-state lithium battery: challenges, progress, and outlook. ACS Appl. Mater. Interfaces 11, 22029–22050.
- Xu, L., Tang, S., Cheng, Y., Wang, K., Liang, J., Liu, C., Cao, Y.C., Wei, F., and Mai, L. (2018). Interfaces in solid-state lithium batteries. Joule 2, 1991–2015.

- van den Broek, J., Afyon, S., and Rupp, J.L.M. (2016). Interface-engineered all-solid-state Liion batteries based on garnet-type fast Li⁺ conductors. Adv. Energy Mater. 6, 1600736.
- 23. Zhu, Y., He, X., and Mo, Y. (2015). Origin of outstanding stability in the lithium solid electrolyte materials: insights from thermodynamic analyses based on first-principles calculations. ACS Appl. Mater. Interfaces 7, 23685–23693.
- 24. Sang, L., Bassett, K.L., Castro, F.C., Young, M.J., Chen, L., Haasch, R.T., Elam, J.W., Dravid, V.P., Nuzzo, R.G., and Gewirth, A.A. (2018). Understanding the ffect of interlayers at the thiophosphate solid electrolyte/lithium interface for all-solid-state Li batteries. Chem. Mater. 30, 8747–8756.
- Adeli, P., Bazak, J.D., Park, K.H., Kochetkov, I., Huq, A., Goward, G.R., and Nazar, L.F. (2019). Boosting solid-state diffusivity and conductivity in lithium superionic argyrodites by halide substitution. Angew. Chem. Int. Ed. 58, 8681– 8686.
- Wang, S., Zhang, Y., Zhang, X., Liu, T., Lin, Y.H., Shen, Y., Li, L., and Nan, C.W. (2018). Highconductivity argyrodite Li₆PS₅Cl solid electrolytes prepared via optimized sintering processes for all-solid-state lithium-sulfur batteries. ACS Appl. Mater. Interfaces 10, 42279–42285
- Ujiie, S., Inagaki, T., Hayashi, A., and Tatsumisago, M. (2014). Conductivity of 70Li₂S+30P₂S₅ glasses and glass-ceramics added with lithium halides. Solid State Ionics 263, 57–61.
- Wu, F., Lee, J.T., Nitta, N., Kim, H., Borodin, O., and Yushin, G. (2015). Lithium iodide as a promising electrolyte additive for lithium-sulfur batteries: mechanisms of performance enhancement. Adv. Mater. 27, 101–108.
- Ujiie, S., Hayashi, A., and Tatsumisago, M. (2012). Structure, ionic conductivity and electrochemical stability of Li₂S-P₂S₅-Lil glass and glass-ceramic electrolytes. Solid State Ionics 211, 42-45.
- Mercier, R., Malugani, J.P., Fahys, B., and Robert, G. (1981). Superionic conduction in Li₂S-P₂S₅-Lil-glasses. Solid State Ionics 5, 663–666.
- Cai, L., Zhao-Yin, W., and Kun, R. (2015). High ion conductivity in garnet-type F-doped Li₇La₃Zr₂O₁₂. J. Inorg. Mater. 30, 995–1001.
- Lu, Y., Meng, X., Alonso, J.A., Fernández-Díaz, M.-A.T., and Sun, C. (2019). Effects of fluorine doping on structural and electrochemical properties of Li_{6.25}Ga_{0.25}La₃Zr₂O₁₂ as

Matter

Article



- electrolytes for solid-state lithium batteries. ACS Appl. Mater. Interfaces 11, 2042–2049.
- Wang, P., Qu, W., Song, W.L., Chen, H., Chen, R., and Fang, D. (2019). Electro-chemomechanical issues at the interfaces in solidstate lithium metal batteries. Adv. Funct. Mater. 29, 1900950.
- Bartsch, T., Strauss, F., Hatsukade, T., Schiele, A., Kim, A.Y., Hartmann, P., Janek, J., and Brezesinski, T. (2018). Gas evolution in all-solidstate battery cells. ACS Energy Lett. 3, 2539– 2543.
- 35. Strauss, F., Teo, J.H., Schiele, A., Bartsch, T., Hatsukade, T., Hartmann, P., Janek, J., and Brezesinski, T. (2020). Gas evolution in lithiumion batteries: solid versus liquid electrolyte. ACS Appl. Mater. Interfaces 12, 20462–20468.
- Mistry, A., and Mukherjee, P.P. (2020). Molar volume mismatch: a malefactor for irregular metallic electrodeposition with solid electrolytes. J. Electrochem. Soc. 167, 082510.
- Tian, H.K., Chakraborty, A., Talin, A.A., Eisenlohr, P., and Qi, Y. (2020). Evaluation of the electrochemo-mechanically induced stress in all-solid-state Li-ion batteries. J. Electrochem. Soc. 167, 090541.
- 38. Larson, J.M., Gillette, E., Burson, K., Wang, Y., Lee, S.B., and Reutt-Robey, J.E. (2018). Pascalammetry with operando microbattery probes: sensing high stress in solid-state batteries. Sci. Adv. 4, eaas8927.
- Fu, C., Venturi, V., Kim, J., Ahmad, Z., Ells, A.W., Viswanathan, V., and Helms, B.A. (2020). Universal chemomechanical design rules for solid-ion conductors to prevent dendrite formation in lithium metal batteries. Nat. Mater. 19, 758–766.
- Xiao, Y., Wang, Y., Bo, S.H., Kim, J.C., Miara, L.J., and Ceder, G. (2020). Understanding interface stability in solid-state batteries. Nat. Rev. Mater. 5, 105–126.
- Ke, X., Wang, Y., Dai, L., and Yuan, C. (2020). Cell failures of all-solid-state lithium metal batteries with inorganic solid electrolytes: lithium dendrites. Energy Storage Mater. 33, 309–328.
- Han, F., Westover, A.S., Yue, J., Fan, X., Wang, F., Chi, M., Leonard, D.N., Dudney, N.J., Wang, H., and Wang, C. (2019). High electronic conductivity as the origin of lithium dendrite formation within solid electrolytes. Nat. Energy 4 (3), 187–196.
- Shen, F., Dixit, M., Xiao, X., and Hatzell, K. (2018). The effect of pore connectivity on Li dendrite propagation within LLZO electrolytes observed with synchrotron X-ray tomography. ACS Energy Lett. 3, 1056–1061.
- Narayan, S., and Anand, L. (2020). On modeling the detrimental effects of inhomogeneous plating-and-stripping at a lithium-metal/solidelectrolyte interface in a solid-state-battery. J. Electrochem. Soc. 167, 040525.
- Klinsmann, M., Hildebrand, F.E., Ganser, M., and McMeeking, R.M. (2019). Dendritic cracking in solid electrolytes driven by lithium insertion. J. Power Sources 442, 227226.
- **46.** Barroso-Luque, L., Tu, Q., and Ceder, G. (2020). An analysis of solid-state electrodeposition-

- induced metal plastic flow and predictions of stress states in solid ionic conductor defects. J. Electrochem. Soc. 167, 020534.
- Tu, Q., Barroso-Luque, L., Shi, T., and Ceder, G. (2020). Electrodeposition and mechanical stability at lithium-solid electrolyte interface during plating in solid-state batteries. Cell Rep. Phys. Sci. 1, 100106.
- Athanasiou, C.E., Jin, M.Y., Ramirez, C., Padture, N.P., and Sheldon, B.W. (2020). Hightoughness inorganic solid electrolytes via the use of reduced graphene oxide. Matter 3, 212–229.
- Kato, A., Yamamoto, M., Sakuda, A., Hayashi, A., and Tatsumisago, M. (2018). Mechanical properties of Li₂S-P₂S₅ glasses with lithium halides and application in all-solid-state batteries. ACS Appl. Energy Mater. 1, 1002– 1007.
- McGrogan, F.P., Swamy, T., Bishop, S.R., Eggleton, E., Porz, L., Chen, X., Chiang, Y.M., and Van Vliet, K.J. (2017). Compliant yet brittle mechanical behavior of Li₂S-P₂S₅ lithium-ionconducting solid electrolyte. Adv. Energy Mater. 7, 1602011.
- Hayashi, A., and Tatsumisago, M. (2018). Mechanical properties of sulfide glasses in allsolid-state batteries. J. Ceram. Soc. Jpn. 126, 719–727.
- 52. LePage, W.S., Chen, Y., Kazyak, E., Chen, K.H., Sanchez, A.J., Poli, A., Arruda, E.M., Thouless, M.D., and Dasgupta, N.P. (2019). Lithium mechanics: roles of strain rate and temperature and implications for lithium metal batteries. J. Electrochem. Soc. 166, A89–A97.
- 53. Lewis, J.A., Javier, F., Cortes, Q., Boebinger, M.G., Tippens, J., Marchese, T.S., Kondekar, N., Liu, X., Chi, M., and Mcdowell, M.T. (2019). Interphase morphology between a solid-state electrolyte and lithium controls cell failure. ACS Energy Lett. 4, 591–599.
- Wang, M.J., Choudhury, R., and Sakamoto, J. (2019). Characterizing the Li-Solid-Electrolyte interface dynamics as a function of stack pressure and current density. Joule 3, 2165– 2178.
- Kasemchainan, J., and Peter, G. (2018). Allsolid-state batteries and their remaining challenges. Johnson Matthey Technol. Rev. 2, 177–180
- Jow, T.R., and Liang, C.C. (1983). Interface between solid anode and solid electrolyte effect of pressure on Li/Lil(Al₂O₃) interface. Solid State Ionics 10, 695–698.
- 57. Garcia-Mendez, R., Mizuno, F., Zhang, R., Arthur, T.S., and Sakamoto, J. (2017). Effect of processing conditions of 75Li₂S-25P₂S₅ solid electrolyte on its DC electrochemical behavior. Electrochim. Acta 237, 144–151.
- 58. Sharafi, A., Haslam, C.G., Kerns, R.D., Wolfenstine, J., and Sakamoto, J. (2017). Controlling and correlating the effect of grain size with the mechanical and electrochemical properties of Li₂La₃Zr₂O₁₂ solid-state electrolyte. J. Mater. Chem. A 5, 21491–21504.
- Cheng, L., Chen, W., Kunz, M., Persson, K., Tamura, N., Chen, G., and Doeff, M. (2015).
 Effect of surface microstructure on electrochemical performance of garnet solid

- electrolytes. ACS Appl. Mater. Interfaces 7, 2073–2081.
- Conder, J., Marino, C., Novák, P., and Villevieille, C. (2018). Do imaging techniques add real value to the development of better post-Li-ion batteries? J. Mater. Chem. A 6, 3304–3327.
- Dixit, M.B., Regala, M., Shen, F., Xiao, X., and Hatzell, K.B. (2018). Tortuosity effects in garnettype Li₇La₃Zr₂O₁₂ solid electrolytes. ACS Appl. Mater. Interfaces 11, 2022–2030.
- 62. Seitzman, N., Guthrey, H., Sulas, D.B., Platt, H.A.S., Al-Jassim, M., and Pylypenko, S. (2018). Toward all-solid-state lithium batteries: three-dimensional visualization of lithium migration in β-Li₂PS₄ ceramic electrolyte. J. Electrochem. Soc. 165, A3732–A3737.
- 63. Haas, R., Pompe, C., Osenberg, M., Manke, I., Maitra, U., and Langsdorf, D. (2019). Practical implications of using a solid electrolyte in batteries with sodium anode: a combined Xray tomography and model-based study. Energy Technol. 7, 1801146.
- 64. Ma, J., Chen, B., Wang, L., and Cui, G. (2018). Progress and prospect on failure mechanisms of solid-state lithium batteries. J. Power Sources 392, 94–115.
- 65. Dixit, M.B., Zaman, W., Hortance, N., Vujic, S., Harkey, B., Shen, F., Tsai, W.Y., De Andrade, V., Chelsea Chen, X., Balke, N., and Hatzell, K.B. (2020). Nanoscale mapping of extrinsic interfaces in hybrid solid electrolytes. Joule 4, 207–221.
- Brissot, C., Rosso, M., and Lascaud, S. (1999). Dendritic growth mechanisms in lithium/ polymer cells. J. Power Sources 81, 925–929.
- Raj, R., and Wolfenstine, J. (2017). Current limit diagrams for dendrite formation in solid-state electrolytes for Li-ion batteries. J. Power Sources 343, 119–126.
- Bonnick, P., Niitani, K., Nose, M., Suto, K., Arthur, T.S., and Muldoon, J. (2019). A high performance all solid state lithium sulfur battery with lithium thiophosphate solid electrolyte. J. Mater. Chem. A 7, 24173–24179.
- Chai, H., and Lawn, B.R. (2007). Edge chipping of brittle materials: effect of side-wall inclination and loading angle. Int. J. Fract. 145, 159–165.
- Zhang, Y., Lee, J.-W., Srikanth, R., and Lawn, B.R. (2013). Edge chipping and flexural resistance of monolithic ceramics. Dent. Mater. 29, 1201–1208.
- Barai, P., Higa, K., and Srinivasan, V. (2017). Lithium dendrite growth mechanisms in polymer electrolytes and prevention strategies. Phys. Chem. Chem. Phys. 19, 20493–20505.
- 72. Masquelier, C. (2011). Solid electrolytes: lithium ions on the fast track. Nat. Mater. 10, 649–650.
- Famprikis, T., Canepa, P., Dawson, J.A., Islam, M.S., and Masquelier, C. (2019). Fundamentals of inorganic solid-state electrolytes for batteries. Nat. Mater. 18, 1278–1291.
- Armstrong, R.D., Dickinson, T., and Turner, J. (1974). The breakdown of β-alumina ceramic electrolyte. Electrochim. Acta 19, 187–192.





- Al-Amleh, B., Lyons, K., and Swain, M. (2010). Clinical trials in zirconia: a systematic review. J. Oral Rehabil. 37, 641–652.
- Choong, Z.J., Huo, D., Degenaar, P., and O'Neill, A. (2019). Micro-machinability and edge chipping mechanism studies on diamond micro-milling of monocrystalline silicon. J. Manuf. Process. 38, 93–103.
- Cao, Y. (2001). Failure analysis of exit edges in ceramic machining using finite element analysis. Eng. Fail. Anal. 8, 325–338.
- 78. Chai, H. (2015). On edge chipping in cylindrical surfaces. Int. J. Sol. Struct. 54, 12–19.
- Nose, M., Kato, A., Sakuda, A., Hayashi, A., and Tatsumisago, M. (2015). Evaluation of mechanical properties of Na₂S-P₂S₅ sulfide glass electrolytes. J. Mater. Chem. A 3, 22061– 22065.
- Hatzor, Y.H., and Palchik, V. (1997). The influence of grain size and porosity on crack initiation stress and critical flaw length in dolomites. Int. J. Rock Mech. Min. Sci. 34, 805–816.

- Yang, J.F., Ohji, T., Kanzaki, S., Díaz, A., and Hampshire, S. (2002). Microstructure and mechanical properties of silicon nitride ceramics with controlled porosity. J. Am. Ceram. Soc. 85, 1512–1516.
- 82. Lu, C., Danzer, R., and Fischer, F.D. (2004). Scaling of fracture strength in ZnO: effects of pore/grain-size interaction and porosity. J. Eur. Ceram. Soc. 24, 3643–3651.
- Carniglia, S.C. (1972). Working model for porosity effects on the uniaxial strength of ceramics. J. Am. Ceram. Soc. 55, 610–618.
- 84. T Krauskopf, B Mogwitz, H Hartmann, DK. Singh, WG. Zeier, and J Janek. The fast charge transfer kinetics of the lithium metal anode on the garnet-type solid electrolyte Li_{6.25}Al_{0.25}La₃Zr₂O₁₂. Adv. Energy Mater. 10 page 2000945.
- Kasemchainan, J., Zekoll, S., Jolly, D.S., Ning, Z., Hartley, G.O., Marrow, T.J., and Bruce, P.G. (2019). Critical stripping current leads to

- dendrite formation on plating in lithium anode solid electrolyte cells. Nat. Mater. 18, 1105–1111.
- De Carlo, F., Xiao, X., and Jacobsen, C. (2014). TomoPy: a framework for the analysis of synchrotron tomographic data. J. Synchrotron Radiat. 21, 1188–1193.
- Münch, B., Trtik, P., Marone, F., and Stampanoni, M. (2009). Stripe and ring artifact removal with combined wavelet-fourier filtering. Opt. Express. 17, 8567–8591.
- Paganin, D., Mayo, S.C., Gureyev, T.E., Miller, P.R., and Wilkins, S.W. (2002). Simultaneous phase and amplitude extraction from a single defocused image of a homogeneous object. J. Microsc. 206, 33–40.
- 89. Schneider, C.A., Rasband, W.S., and Eliceiri, K.W. (2012). NIH image to ImageJ: 25 Years of image analysis. Nat. Methods 9, 671–675.
- Munch, B., and Holzer, L. (2008). Contradicting geometrical concepts in pore size analysis attained with electron microscopy and mercury intrusion. J. Am. Ceram. Soc. 91, 4059–4067.